Remote Sensing of Environment 333 (2026) 115110

Contents lists available at ScienceDirect

Remote Sensing of Environment

journal homepage: www.elsevier.com/locate/rse

Automated drone-borne GPR mapping of root-zone soil moisture for precision irrigation

Kaijun Wu [a], Jean Artois [b], Denis Tourneur [b], Merlin Mareschal [a], Maud Henrion [a], Sashini Pathirana [c], Lakshman Galagedara [c], Quentin Limbourg [b], Sébastien Lambot [a,*]

[a] Université catholique de Louvain, Earth and Life Institute, Environmental Sciences, Louvain-la-Neuve, Belgium
[b] Centre Wallon de Recherches Agronomiques, Département Productions Agricoles, Gembloux, Belgium
[c] School of Science and the Environment, Memorial University of Newfoundland, Corner Brook, Newfoundland and Labrador, Canada

ARTICLE INFO

Edited by Jing M. Chen

Keywords:
Drone-borne GPR
Smart irrigation
Time-lapse monitoring
Root-zone soil moisture
Soil water content
Precision agriculture

ABSTRACT

High-resolution monitoring of root-zone soil moisture is essential for optimizing irrigation in precision agriculture. This study demonstrates the potential of drone-borne Ground-Penetrating Radar (GPR) to map spatial and temporal soil moisture dynamics across an agricultural field over an entire growing season. Using the innovative gprSense® system, which combines a frequency-domain radar with full-wave inversion, we achieved precise and automated data acquisition and processing. To our knowledge, this is the first study to implement time-lapse, root-zone soil moisture mapping using drone-borne GPR combined with real-time full-wave inversion. Time-lapse mapping was conducted in a spinach field, yielding eight high-resolution soil moisture maps that captured dynamic variations driven by precipitation and irrigation. Operating in the frequency range 110–120 MHz, the system measured soil moisture down to a depth of approximately 35–40 cm, with comparisons performed using Time Domain Reflectometry (TDR) sensors and mass balance analyses. Electrical Resistivity Tomography (ERT) provided complementary data into soil electrical conductivity patterns. Results revealed strong agreement between GPR-derived soil moisture estimates and conventional methods, with spatial patterns aligning closely with predictions from Boosted Regression Tree (BRT) models. These findings demonstrate the capacity of drone-borne GPR to deliver actionable, root-zone scale insights for real-time irrigation optimization and agricultural water management.

1. Introduction

In the realm of precision agriculture, optimizing water resources poses a critical challenge, particularly given increasing climatic variability and the pressing demand for sustainable farming practices (Wallace, 1994; Seyedmohammadi et al., 2016; Falloon et al., 2011; Bwambale et al., 2022). Effective soil moisture monitoring is essential for efficient irrigation management, as it directly influences crop yield, water use efficiency, and the overall health of agricultural ecosystems (Chatterjee et al., 2022; Yavkacheva, 2023).

Traditional methods for assessing soil moisture, while accurate to some extent, often fail to provide the timely, spatially detailed data required for precision agriculture (Vereecken et al., 2008; Dobriyal et al., 2012; Sharma et al., 2018). For instance, the gravimetric method is considered a standard reference for soil moisture measurement due to its high accuracy. However, it is labor-intensive, time-consuming, and requires soil sample collection, drying, and weighing. Furthermore, the inherent spatial variability of soil moisture at the field scale renders point-based soil sampling unrepresentative of larger areas. Time Domain Reflectometry (TDR) and capacitive sensors offer accurate measurements at specific depths and are suitable for both laboratory and field applications. However, these methods are intrusive and only provide localized measurements, making them similarly inadequate for capturing field-scale conditions. Satellite remote sensing, while valuable for monitoring soil moisture over large areas, suffers from limited spatial resolution and is typically restricted to surface soil moisture. Additionally, satellite observations, often operating in high-frequency bands such as L- and C-bands, are prone to noise, clutter, surface roughness, and vegetation interference (Paloscia et al., 2013; Bauer-Marschallinger et al., 2019; El Hajj et al., 2017; Misra et al., 2020; Varghese et al., 2021).

Ground-penetrating radar (GPR) has emerged as a powerful tool for

* Corresponding author.
E-mail address: sebastien.lambot@uclouvain.be (S. Lambot).

https://doi.org/10.1016/j.rse.2025.115110
Received 21 February 2025; Received in revised form 25 August 2025; Accepted 26 October 2025
Available online 5 November 2025

field- scale soil moisture characterization (Galagedara et al., 2003; Huisman et al., 2003; Lambot et al., 2004, 2008; Minet et al., 2012; Mahmoudzadeh Ardekani, 2013; Tran et al., 2015; Klotzsche et al., 2018; Ercoli et al., 2018; Zhou et al., 2019; Pathirana et al., 2023). By providing high-resolution, field-scale data, GPR addresses the gap between traditional on-ground measurements and satellite remote sensing, aligning with scales relevant to agricultural management. Traditionally, GPR has been deployed manually or on ground-based platforms, such as quads, enabling automated, high-resolution soil moisture mapping over relatively large fields (Minet et al., 2012). However, ground- based platforms face significant operational challenges in crop-covered fields, where access is restricted, and deployment becomes labor-intensive and time- consuming.

Recent advancements in drone technology have enabled GPR to be deployed on lightweight aerial platforms, allowing for rapid, high-resolution soil moisture mapping over larger areas while avoiding disturbance to vegetation. In Wu et al. (2019), we showcased the potential of drone-borne GPR for precision agriculture by demonstrating its application in soil moisture mapping. Our approach employs the full-wave radar equation (Lambot et al., 2004; Lambot and André, 2014), with soil dielectric permittivity, directly correlated with soil moisture, retrieved through full-wave inversion focused on the surface reflection in the time domain. Notably, radar-drone interactions are intrinsically incorporated in the radar equation, except for the small effects of dynamic propellers, ensuring precise soil moisture estimates. The full-wave inversion method has already been rigorously validated under controlled conditions (Lambot et al., 2004, 2006b; Anh Phuong et al., 2014) and further confirmed at the field scale, notably in Lambot et al. (2008); Minet et al. (2012), which provided comprehensive validation for soil moisture mapping. Building on these validations, the approach has also been applied in diverse field studies (Tran et al., 2015; Wu et al., 2019), demonstrating its robustness across contrasting soils and environmental conditions.

Drone-mounted GPR systems have demonstrated their versatility across a wide range of applications. For instance, Valence et al. (2022) combined Time Domain Reflectometry (TDR) and drone-mounted GPR measurements to map and analyze snowpack composition in mountainous regions, enhancing our understanding of the effects of rain-on-snow events. Similarly, Sipos and Gleich (2020) developed a lightweight, energy-efficient GPR system for drones, optimized to detect buried landmines in challenging terrain. For civil engineering applications, Frid and Frid (2024) showed how drone-mounted GPR can effectively map underground water levels, delivering critical insights for infrastructure planning and maintenance.

Additional studies have explored drone-mounted GPR systems for environmental and agricultural applications (Cheng et al., 2023; Pramudita et al., 2022). For instance, Pramudita et al. (2022) investigated the influence of vegetation on soil moisture measurements using an L-band radar mounted on a drone, developing methods to correct for vegetation effects on radar wave propagation, thereby improving measurement accuracy. Similarly, Cheng et al. (2023) presented a drone-mounted GPR approach to estimate surface soil moisture across varying elevations, showing strong agreement with traditional techniques such as TDR. Nevertheless, these approaches often rely on simplifying assumptions in their data processing methods, which can limit their usability for non-GPR experts and potentially introduce estimation errors.

Further advancements in drone-borne GPR, such as those by Wu et al. (2022); Wu and Lambot (2022b), have investigated factors affecting measurement accuracy, including soil roughness and incident angle. These influences can be minimized by operating at lower frequencies and using a half-wave dipole antenna, which is less directive. Numerical sensitivity analyses by Lambot et al. (2006b) and Wu and Lambot (2022a) have highlighted how measurement depth depends on frequency and soil layering, emphasizing the importance of further investigation using field data to validate these insights.

In this study, we aimed to evaluate the potential of drone-borne GPR for high-resolution, time-lapse monitoring of root-zone soil moisture in an agricultural field during a spinach growing season. Specifically, we deployed the gprSense® system (www.gprsense.com), a lightweight prototype radar designed for scientists and farmers alike, which features automated data acquisition and full-wave inversion. Time Domain Reflectometry (TDR) sensors were installed at multiple depths to provide independent reference data for comparison with the GPR-based soil moisture maps. Additionally, Electrical Resistivity Tomography (ERT) was conducted to assess soil variability across the field. We analyzed soil moisture dynamics in response to precipitation and irrigation events, and used Boosted Regression Tree (BRT) models to evaluate and interpret spatial patterns of soil moisture distribution across the field.

This study represents a significant step forward in drone-based soil moisture mapping by demonstrating, for the first time, high-resolution, time-lapse monitoring of root-zone soil water content using a drone-borne GPR system with real-time full-wave inversion. Unlike previous studies that focused on surface moisture or used simplified retrieval techniques, our work integrates a complete, physically based radar model, validated in a large number of earlier studies, into a lightweight, automated platform capable of operational deployment in agricultural fields. This unique configuration enables non-invasive, spatially continuous monitoring of root-zone dynamics with minimal human intervention, addressing key limitations of existing in-situ, remote sensing, and modeling approaches.

While drone-borne Ground-Penetrating Radar (GPR) holds significant promise for precision agriculture, its widespread adoption will require regulatory adaptations to enable its full potential. In many regions, GPR operations are restricted to altitudes below one meter above ground level, limiting deployment flexibility. As regulations evolve, addressing these constraints will be essential to fully harness the capabilities of drone-based GPR systems in agricultural applications, thereby providing farmers and scientists with practical tools for optimizing water management. In this study, the system operates under the GPR regulatory class and emits low-power, sparsely sampled, discrete-frequency continuous-wave signals using standard vector network analyzer technology. Operating in close proximity to the ground, it minimizes the risk of potential interference with other electromagnetic systems.

2. Methodology

2.1. Overview and workflow

The objective of this study was to generate high-resolution, time-lapse root-zone soil moisture (SWC) maps using an innovative drone-borne Ground-Penetrating Radar (GPR) system, based on frequency-domain radar and full-wave inversion. The methodology comprises four main steps: (i) automated GPR data acquisition via drone, (ii) radar–drone calibration, (iii) full-wave inversion to retrieve soil dielectric properties, and (iv) conversion to volumetric water content and spatial interpolation. While based on established and validated theoretical frameworks (Lambot et al., 2004, 2006b; Minet et al., 2012; Wu et al., 2019, 2022), the implementation is novel in its real-time, fully automated operation and its ability to generate high-resolution, time-lapse root-zone moisture maps under real field conditions. This proof of concept opens promising avenues for digital soil mapping, such as precision irrigation support and validation of satellite soil moisture products. Fig. 1 presents the complete radar data processing workflow. This pipeline is fully automated in the gprSense® software, enabling seamless integration from data acquisition to final mapping.

2.2. Drone-based data acquisition

We used the Tundra drone (Hexadrone, Saint-Ferréol-d'Auroure, France), equipped with a 5 GHz rangefinder for close terrain following,

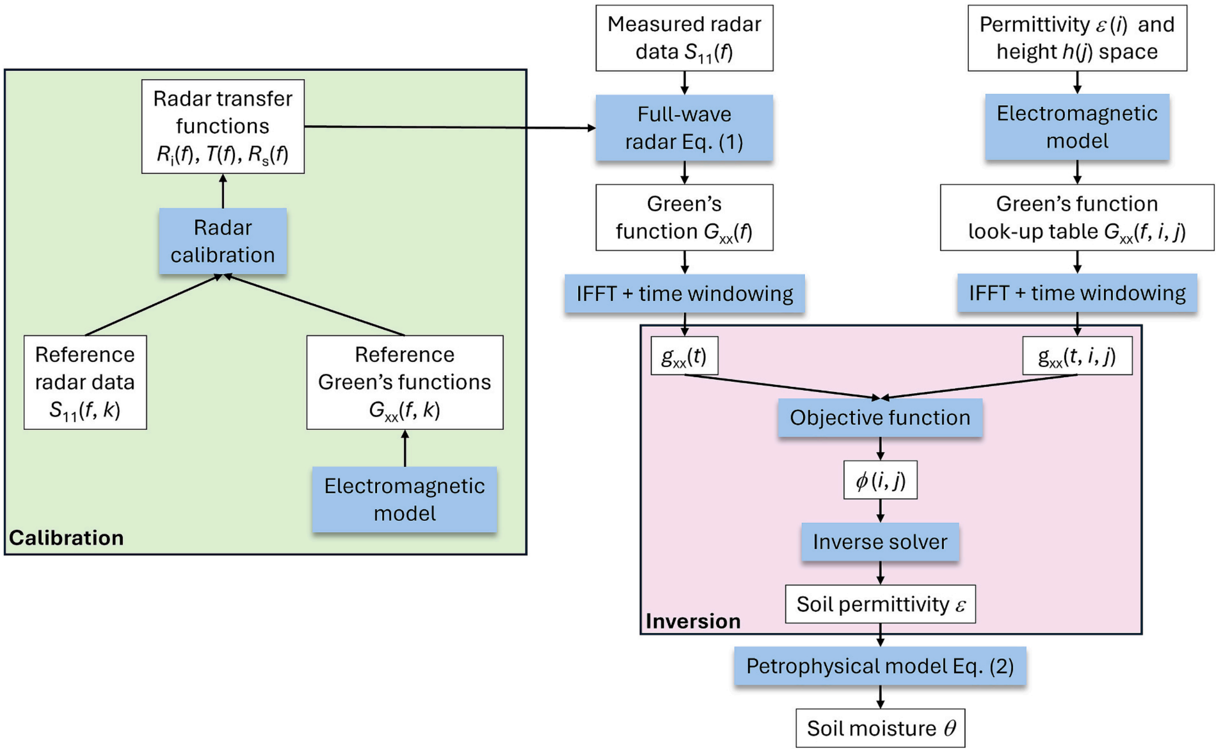

Fig. 1. Workflow of the full-wave radar data processing implemented in the gprSense® system for drone-borne soil moisture estimation. This figure, adapted from the gprSense® user manual (version 1.0.0, 2025), presents the first complete integration of radar calibration, full-wave time-domain inversion using a precomputed look-up table, and automated mapping of volumetric water content within a drone-compatible radar instrument.

to carry the 2.4 kg radar system. The drone followed parallel flight lanes spaced 6 meters apart to ensure full coverage of the field. With an average flight speed of approximately 12.5 km/h and a radar acquisition rate of 7.5 Hz, this results in approximately two measurements per meter along each flight line. Combined with the inversion process and kriging interpolation, the GPR-derived soil moisture maps offer a high spatial resolution suitable for capturing fine-scale variability relevant to irrigation management.

2.3. Radar system

The gprSense® radar system (www.gprsense.com) is a frequency-domain instrument optimized for drone operations (Fig. 2). For root-zone characterization, it employs a 110–120 MHz dipole antenna. This frequency range provides an effective trade-off between sensing depth and reduced sensitivity of the surface reflection to soil electrical conductivity. Indeed, lower frequencies enable deeper penetration but increase the influence of conductivity (Lambot et al., 2006b; Wu and Lambot, 2022a). The radar is equipped with a differential GPS for positioning and a control unit for data acquisition and onboard processing (edge computing). The dipole antenna provides a quasi-isotropic radiation pattern for small angular deviations, particularly in the horizontal (H) plane, where it is theoretically uniform, thereby minimizing angular sensitivity to typical drone pitch and roll motions (Wu and Lambot, 2022b).

2.4. Full-wave inversion and soil moisture estimation

The full-wave radar equation used for inversion is (Lambot et al., 2004; Lambot and André, 2014):

$$S_{11}(\omega) = R_i(\omega) + \frac{T(\omega)G_{xx}(\omega)}{1 - G_{xx}(\omega)R_s(\omega)} \quad (1)$$

Fig. 2. Drone-borne mapping of root-zone soil moisture on the test site using the gprSense® system (www.gprsense.com), mounted on a Tundra drone from Hexadrone (Saint-Ferréol-d'Auroure, France). The photograph shows the 2024 version of the instrument, while the data presented in this study were collected with an earlier 2023 version. The gentle slope toward the talweg is visible in the background.

where $S_{11}(\omega)$ is the measured reflection coefficient, ω is the angular frequency, and $G_{xx}(\omega)$ is the Green's function of the medium, i.e., the exact solution of Maxwell's equations for wave propagation in three-dimensional layered media (Chew, 1995; Slob and Fokkema, 2002). The terms $R_i(\omega)$, $T(\omega)$, and $R_s(\omega)$ are the system's transfer functions, representing internal radar reflections, antenna transmission, and antenna–medium interactions, respectively.

Radar calibration consists in determining the transfer functions $R_i(\omega)$, $T(\omega)$, and $R_s(\omega)$. In our setup, the complete radar–drone system is calibrated as a whole, treating the drone as an integral part of the radar system to implicitly account for radar–drone interactions. Calibration measurements were performed at multiple heights above a known reference medium, specifically, a deep lake, as described in Wu and Lambot (2022a). The corresponding Green's functions $G_{xx}(\omega)$, representing the theoretical water-surface reflection responses, were simulated. Based on these simulations and the measured $S_{11}(\omega)$, the system's transfer functions were estimated by solving a linear system of equations, as detailed in Lambot et al. (2004, 2006a). Calibration was performed once and considered valid over the entire experimental period. While a temperature-dependent radar calibration was not available at the time of the experiment, it has since been implemented in version 1.0.0 of gprSense®.

Although the radar operates in the frequency domain, the inversion was performed in the time domain to isolate the early-time surface reflection and improve estimation robustness (Lambot et al., 2006b). Inversion was implemented using a least-squares optimization in the time domain. A precomputed look-up table (LUT) of Green's functions was generated for a range of permittivity values, allowing real-time matching with measured data. The retrieved relative permittivity ε_r at each trace location was then converted to volumetric water content θ using Topp's empirical equation (Topp et al., 1980), which is widely accepted as valid for mineral soils, including the loamy soil at the study site:

$$\theta = -5.3\times10^{-2} + 2.92\times10^{-2}\varepsilon_r - 5.5\times10^{-4}\varepsilon_r^2 + 4.3\times10^{-6}\varepsilon_r^3 \quad (2)$$

2.5. Mapping and interpolation

The volumetric water content values were interpolated spatially using ordinary Kriging. For each acquisition date, the georeferenced estimates were interpolated to produce a high-resolution spatial map of root-zone soil moisture, with a final grid resolution of 1 m. This allowed detailed visualization of spatial patterns across the field. The entire processing workflow was repeated across eight acquisition dates spanning the growing season, enabling time-lapse monitoring of soil moisture dynamics under varying irrigation and climatic conditions.

2.6. Electrical resistivity tomography

Electrical Resistivity Tomography (ERT) was applied to map the soil electrical resistivity and its related conductivity at the test site. In this study, we used the Veris Q2800 system (Veris Technologies, Salina, KS, United States) (Fig. 3). The Veris Q2800 system is equipped with six disk-shaped electrodes, allowing non-invasive measurement of apparent soil resistivity at depths ranging from 30 cm to 90 cm, with readings taken every second. To ensure comparability with the radar-derived root-zone estimates, only results corresponding to the 30 cm depth are presented in this paper.

Fig. 3. Mapping soil electrical conductivity using Electrical Resistivity Tomography (ERT) with the Veris Q2800 system (Veris Technologies, Salina, KS, USA) towed by an all-terrain vehicle (ATV). The system provides measurements at two depths: 30 cm and 90 cm.

2.7. Boosted regression trees

To complement the radar-based retrievals, we implemented a Boosted Regression Tree (BRT) model to estimate soil moisture based on terrain and soil conductivity variables. This indirect approach, commonly used in digital soil mapping, provides a practical reference to explore spatial patterns of soil water content using easily accessible environmental predictors. While not as precise as the GPR-based method, it offers valuable supplementary insights into field-scale heterogeneity and helps support the interpretation of the spatial variability observed in the radar-based maps.

BRT combines multiple decision trees into an ensemble model using boosting, iteratively improving predictions by minimizing errors from previous iterations. This approach is particularly effective for modeling non-linear relationships and interactions between variables, making it well-suited for spatial prediction tasks. Additionally, BRT provides estimates of variable importance, offering insights into the influence of individual predictors on the model's performance. Specifically, it utilized altitude, flow accumulation index, slope, and electrical conductivity (Tarboton, 1997). These parameters were computed using the digital terrain model (DTM) from the Géoportail de la Wallonie, available on WalOnMap (https://geoportail.wallonie.be/), acquired on March 2nd, 2021. Soil electrical resistivity and its associated conductivity were obtained using the Veris Q2800 system, as described in the previous section (Fig. 3).

A 6-fold cross-validation procedure was applied to parameterize the degree of complexity of the model (Elith et al., 2008). Due to spatial auto-correlation, training and validation data are rarely independent. To address this, the data were spatially divided into 41 blocks and subsequently allocated randomly into 6 folds (Valavi et al., 2019). The model's reliability was assessed using the Root Mean Square Error (RMSE) and Pearson Correlation Coefficient between the model predictions and the dependent variable. These metrics were calculated for the full dataset (self-statistic) and averaged over each fold in the Cross-Validation (CV) process (CV statistics).

2.8. Correlation coefficient and root mean square error

For quantitative analysis, the Root Mean Square Error (*RMSE*) and correlation coefficient (*r*) were used to compare the relevant results. These metrics are formulated as follows:

$$RMSE = \sqrt{\sum_{n=1}^{N}\frac{(x_n - y_n)^2}{N}} \quad (3)$$

$$r = \frac{\sum_{n=1}^{N}(x_n-\overline{x})(y_n-\overline{y})}{\sqrt{\sum_{n=1}^{N}(x_n-\overline{x})^2\sum_{n=1}^{N}(y_n-\overline{y})^2}} \quad (4)$$

Here, x_n and y_n are the nth values in the x and y variables, respectively, and N is the total number of data points. $\overline{x}$ and $\overline{y}$ represent the means of the x and y variables.

3. Agricultural field test site and measurements overview

The study was conducted in a 5.72-hectare agricultural field located in the central Belgian loess belt (50°32'15.44"N, 4°49'11.19"E), characterized by predominantly sandy-loam and silt-loam soils (Fig. 4). This region is a significant agricultural area, with 65% of the land cover dedicated to cropland (Evrard et al., 2008). In the years prior to this

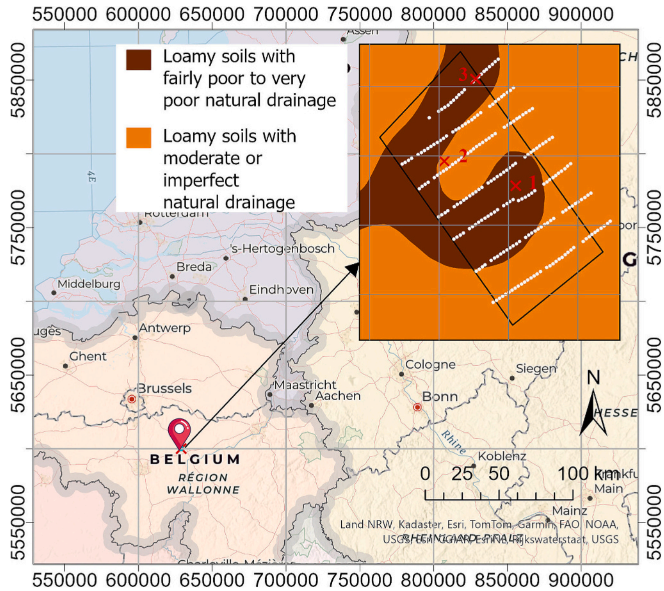

Fig. 4. Study area in a 5.72-ha agricultural field in Belgium. White dots indicate the positions of rain gauges, and red cross markers indicate the positions of TDR sensors. Soil type data are sourced from the Géoportail de la Wallonie (https://geoportail.wallonie.be). Coordinates are in WGS 1984-UTM Zone 31 N.

study, the field was cultivated with potatoes, spelt, and onions. In 2023, spinach was sown and subsequently harvested on August 14th and September 23rd. During the last spinach growing season of the year, time-lapse drone-borne GPR and TDR measurements were conducted, with all relevant data recorded for comprehensive analysis.

The slope, altitude, and flow accumulation index of the site are shown in Fig. 5(a), (b), and (c), respectively. The test site is slightly undulating, with a maximum slope of approximately 10° (Fig. 5(a)) and a height difference of about 13 m (Fig. 5(b)). The field presents a general slope in the northwest direction. A talweg is present in the northwest portion of the field, which naturally accumulates more water. The edge of the site follows a large flow stream, with some branches extending toward the center of the field (see Fig. 5(c)).

Electrical Resistivity Tomography (ERT) measurements were conducted only once, on April 21st, 2023, due to the partly intrusive nature of the method, which precluded measurements during the growing season. The soil electrical conductivity map is presented in Fig. 6, highlighting the variability of soil properties. Most of the field exhibits relatively low electrical conductivity, with a small area of higher conductivity observed in the northwest corner, corresponding to the talweg.

Rain gauges and TDR sensors were installed horizontally on the site for in-situ monitoring. Three TDR profiles were set up at the site, marked as the red cross markers N°1, 2, and 3 in Fig. 4, to measure soil water content at depths of 10, 20, 30, 40, 50, and 60 cm, respectively. Rain gauges, located at various positions (white dots in Fig. 4), recorded the total water received, including precipitation and irrigation, during September 14th and 15th. The irrigation system, consisting of an Irrimec hose reel and cannons, was monitored using the Raindancer application (https://www.raindancer.com/). This application retrieved the GPS coordinates of the start and end of each irrigation line and recorded the amount of water applied (in mm) for each irrigation event.

The drone-borne GPR was operated on August 22nd, 25th, and 29th, as well as on September 5th, 8th, 11th, 15th, and 20th, resulting in a total of eight time-lapse soil water content (SWC) maps. Daily meteorological data were obtained from the Sencrop weather station (https://sencrop.com) installed in the northwest portion of the plot. The station is equipped with a rain gauge, thermometer, and anemometer, providing daily data on precipitation, temperature, wind speed, and

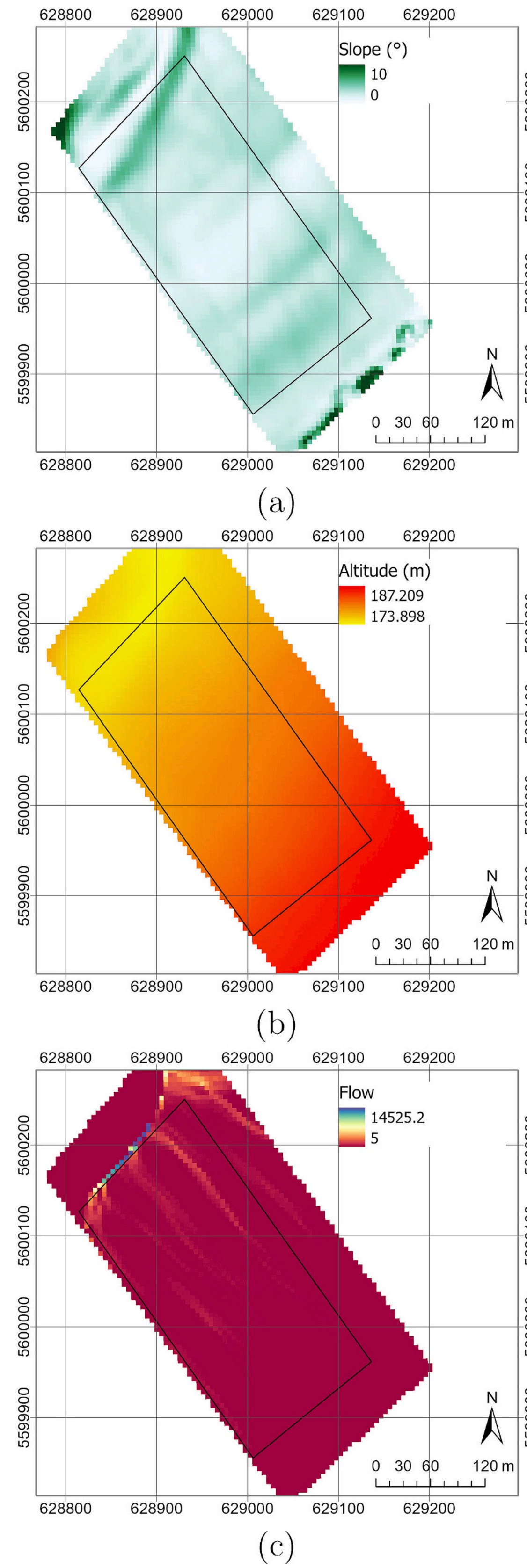

Fig. 5. Maps of slope (a), altitude (b), and flow accumulation index (c) from the Géoportail de la Wallonie (https://geoportail.wallonie.be). Coordinates are in WGS 1984-UTM Zone 31 N.

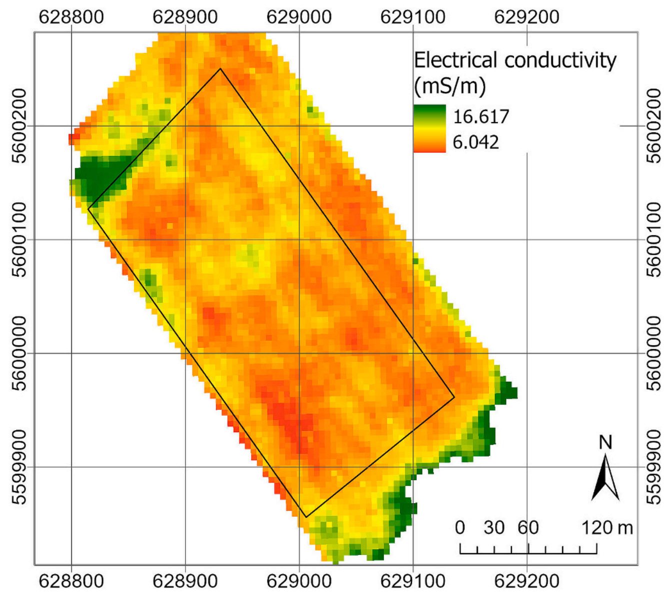

Fig. 6. Electrical conductivity map obtained using the Veris Q2800 system on April 21st, 2023. Coordinates are in WGS 1984-UTM Zone 31 N.

other weather parameters for the field. It is important to note that the daily rainfall data from Sencrop provide general information for the entire test site and differ from the rain gauge measurements taken at specific locations within the field (white dots in Fig. 4).

4. Results and discussion

4.1. Time-lapse soil moisture

Soil moisture maps measured by the drone-borne GPR are presented in Fig. 7. Fig. 8 shows the time-series results, including the mean values of soil water content measured by the GPR, precipitation, irrigation, and air temperature as functions of the date. Irrigation events were manually recorded in the Sencrop application as they occurred.

From Fig. 7, the site was relatively wet on August 25th and 29th. A small wet area is consistently visible in the northwest corner of the maps in Fig. 7(d)-(h), aligning with the high conductivity area shown in Fig. 6. This area corresponds to the talweg in the topography, as previously highlighted. As shown in Fig. 8, the mean soil water content closely corresponds to rainfall and irrigation events. For instance, a relatively heavy rainfall on August 24th increased soil moisture from approximately 0.23 on August 22nd to above 0.35. In contrast, soil moisture decreased steadily on September 5th, 8th, and 11th due to increased air temperature, evapotranspiration and root water uptake, drainage, and the absence of rainfall or irrigation between September 2nd and 11th (Fig. 8).

The time-series soil moisture results measured by TDR are presented in Fig. 9. Notably, TDR N°1 shows local maxima in soil moisture values during the early afternoon, such as around 13:00 on September 10th, 11th, 12th, 16th, and 17th. In contrast, the values recorded by TDR N°2 and N°3 at the other two positions remain relatively stable, except for the 10 cm depth at TDR N°2. Additionally, soil moisture at 10 and 20 cm depths is highest at the position of TDR N°1, whereas the highest moisture levels at TDR N°2 and N°3 occur at greater depths—specifically, 50 cm for TDR N°2 and 60 cm for TDR N°3 (with 60 cm depth not recorded for TDR N°2).

We compared the soil moisture values measured by TDR at different

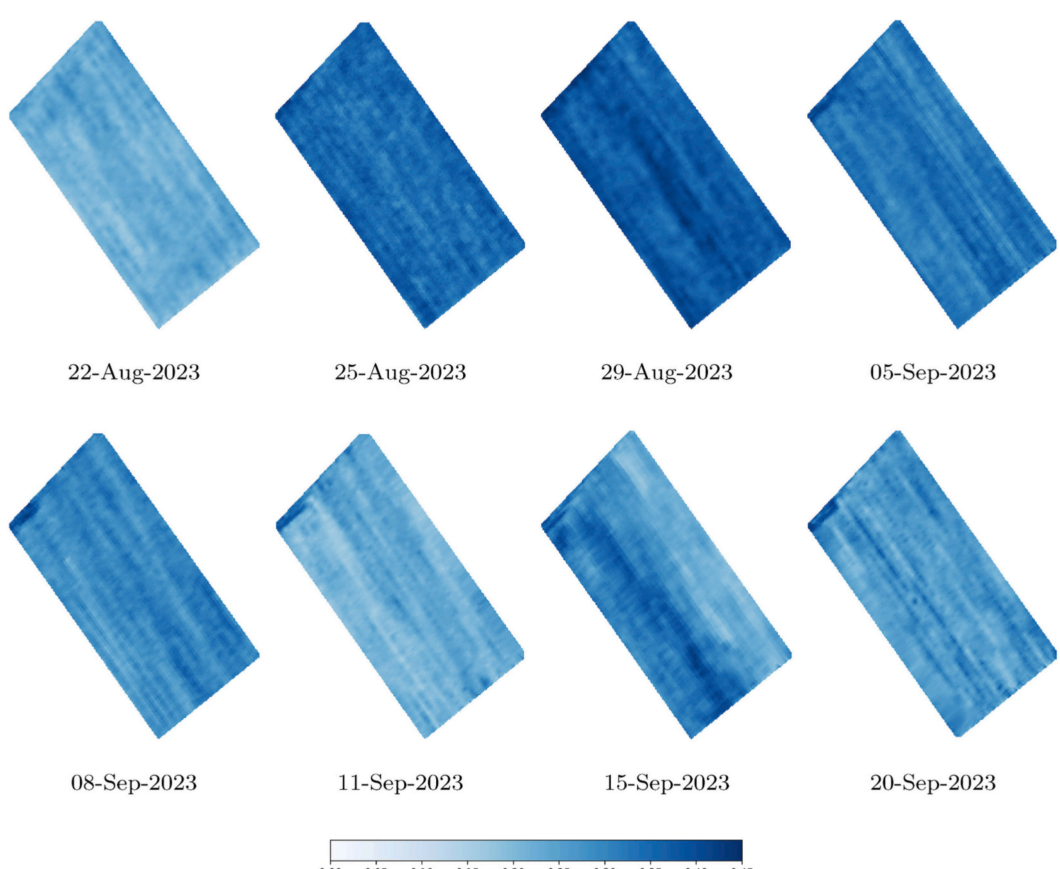

Fig. 7. Volumetric soil moisture maps obtained by the drone-borne GPR. The subcaptions denote the measurement dates. Soil moisture is dimensionless.

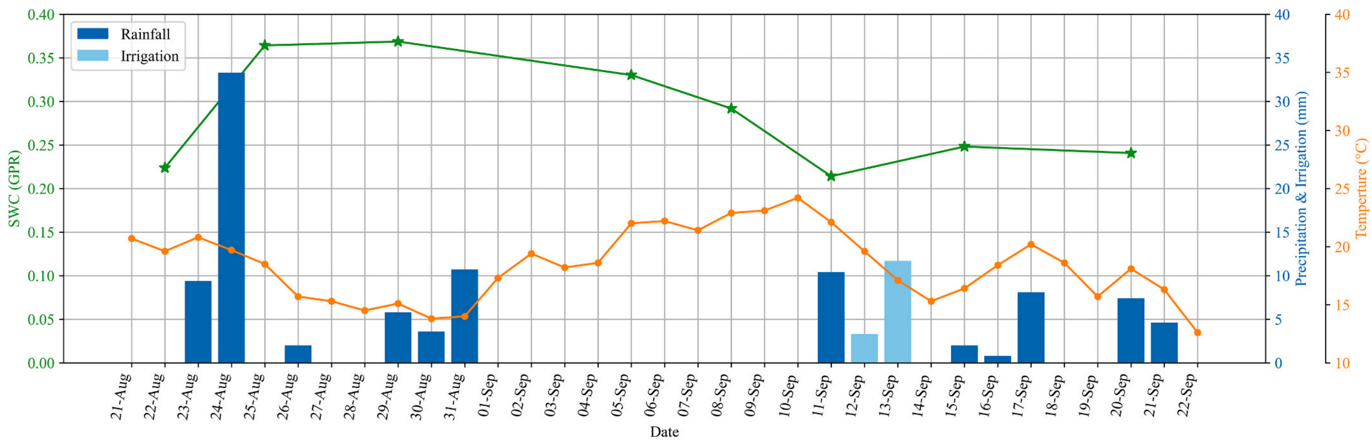

Fig. 8. Time-series observations from the drone-borne GPR. Green stars represent the mean soil water content (SWC) values for each measurement date. Orange dots indicate the daily air temperature. Dark blue bars show the general rainfall for the area, while light blue bars represent irrigation activities at the test site. Temperature and rainfall data were provided by the Sencrop application.

depths with those obtained from the drone-borne GPR, as shown in Fig. 10. Note that the GPR and TDR measurements were not acquired at exactly the same locations, with estimated horizontal offsets of a few meters, which contribute to the observed differences given the inherent variability in the field. A negative correlation ($r = -0.6031$) is observed at 10 cm depth, while higher correlations are found at 30 cm, 40 cm, and 50 cm depths, with the strongest agreement at 30 cm ($r = 0.7688$). The negative correlation observed between GPR-derived and TDR-measured soil water content at 10 cm depth is likely due to the rapid dynamics of surface moisture. Shallow soil layers are highly responsive to atmospheric fluxes, particularly evapotranspiration, which can quickly deplete moisture after irrigation or rainfall. In contrast, the GPR signal reflects an integrated response with sensitivity extending to deeper layers (approximately 30–40 cm), which retain moisture longer. As a result, depending on the atmospheric conditions history, surface drying may coincide with sustained moisture at depth, leading to an inverse relationship between the two measurements.

In addition to the Pearson correlation coefficients, RMSE values were calculated to evaluate the accuracy of GPR-derived soil moisture compared to TDR measurements. The RMSE was lowest at 60 cm depth (0.0582 m^3/m^3), but this result is based on only four TDR measurements, as TDR N°2 did not provide data at this depth (see Fig. 9b). The next lowest RMSE was observed at 50 cm (0.1021 m^3/m^3), followed by 20 cm (0.1064 m^3/m^3), 40 cm (0.1165 m^3/m^3), and 30 cm (0.1188 m^3/m^3), aligning reasonably well with the expected radar characterization depth of 35–40 cm. The highest RMSE occurred at 10 cm depth (0.1319 m^3/m^3), where the correlation with GPR-derived values was also negative.

The differences between TDR and GPR measurements can be attributed to the definition of measurement depth, as well as the slightly different locations where GPR and TDR data were acquired, the micro-variability in the field, and the kriging uncertainty. TDR sensors measure soil water content at specific insertion depths, whereas the GPR provides an effective cumulative response from all soil layers up to approximately 30–40 cm depth, depending on the permittivity and conductivity distribution.

4.2. Empirical determination of GPR characterization depth

The theoretical characterization depth of GPR operating in the 110–120 MHz frequency range, with inversion focused on the surface reflection, is approximately 40 cm. This depth corresponds to a fraction of the wavelength in the soil (Lambot et al., 2006b). To refine this estimate, we employed an empirical approach using the time-lapse GPR measurements from the gprSense® system. These measurements captured soil water content (SWC) variations before and after specific precipitation and irrigation events (Fig. 7). The empirical characterization depth was estimated using a mass balance approach, quantifying the total water input from precipitation and irrigation alongside the corresponding increase in average SWC measured by the GPR.

The mass balance equation is expressed as:

$$\overline{\theta}_{after} \bullet z - \overline{\theta}_{before} \bullet z = q \tag{5}$$

where $\overline{\theta}_{after}$ and $\overline{\theta}_{before}$ are the mean SWC values measured by the GPR after and before precipitation or irrigation, respectively. The term q represents the total water input from precipitation or irrigation (in mm) over the period of interest, and z represents the effective characterization depth (in mm) of the GPR.

Rearranging the equation to solve for z gives:

$$z = \frac{q}{\overline{\theta}_{after} - \overline{\theta}_{before}} \tag{6}$$

Based on multiple events and measurements, the experimentally determined characterization depth for the drone-borne GPR operating in the 110–120 MHz frequency range was approximately 35 cm. It is important to note that evapotranspiration was not accounted for in this analysis. To minimize its influence, only data collected during relatively short periods between GPR measurements and precipitation or irrigation events, where evapotranspiration could be considered negligible, were used.

While we refer to a “characterization depth” for practical interpretation, as in satellite remote sensing applications, it is important to recognize that this concept does not correspond to a strict physical boundary. In our inversion model, the medium is treated as a homogeneous half-space, and the inversion is focused on the surface reflection. The measured signal corresponds to the integrated response from vertical variations in permittivity within the radar’s sensitivity range. As described in Lambot et al. (2006b), vertical contrasts near the interface can generate constructive or destructive interference effects, which contribute to the net reflected waveform. These interferences, shaped by the contrast amplitude and the wavelength, can result in either overestimation or underestimation of soil moisture. Consequently, the radar response is best interpreted in terms of a sensitivity profile rather than a fixed depth. Nonetheless, for practical applications and comparisons, the “characterization depth”, approximately 35–40 cm in this study, is commonly used as an effective estimate of the soil depth range contributing most to the reflected signal. This depth is not universal, as it also depends on soil electromagnetic properties such as permittivity and conductivity, and may vary under drier or wetter conditions. In practical irrigation applications, however, soil conditions are rarely extremely

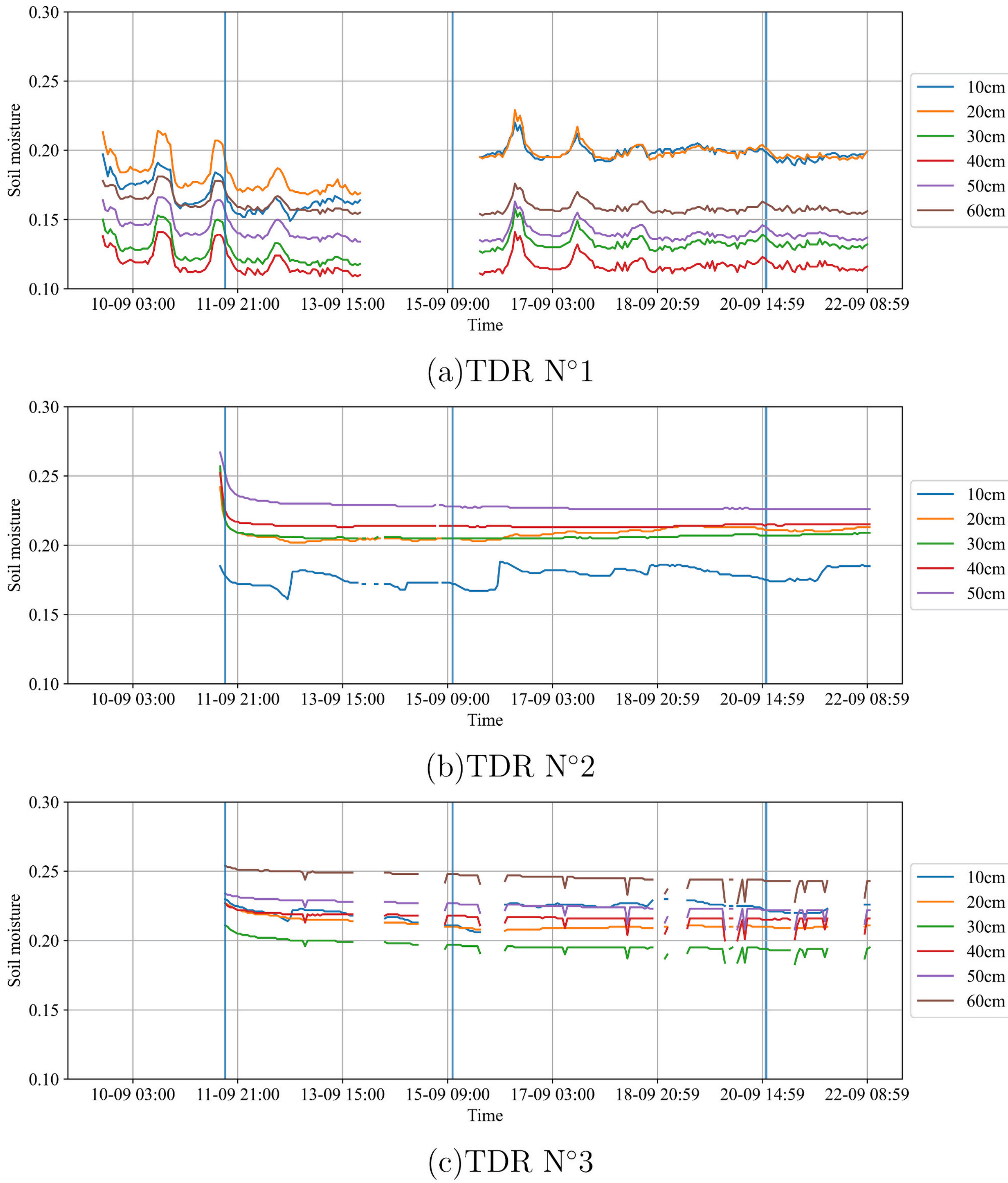

Fig. 9. Time-series observations of soil moisture (dimensionless) from the three TDR sensors at three positions on the site (see Fig. 4). The legend indicates the depth of the sensors. Blue vertical bars represent the measurement times of the drone-borne GPR.

dry, as maintaining sufficient moisture is essential for plant health and productivity. Therefore, the characterization depth estimated under wet or moist conditions, as in this study, is particularly relevant for irrigation management and decision-making.

4.3. *Specific soil moisture maps*

In this analysis, we selected the soil moisture maps measured on September 11th and 15th (see Fig. 7(f) and (g)) for further investigation. These two moisture maps were compared with predictions from other methods and available information.

4.3.1. *Comparison with BRT prediction*

The BRT method was used to predict the soil water content (SWC) map, and the results were compared with the GPR-derived SWC map. We focused on the measurements from September 11th, as this date was

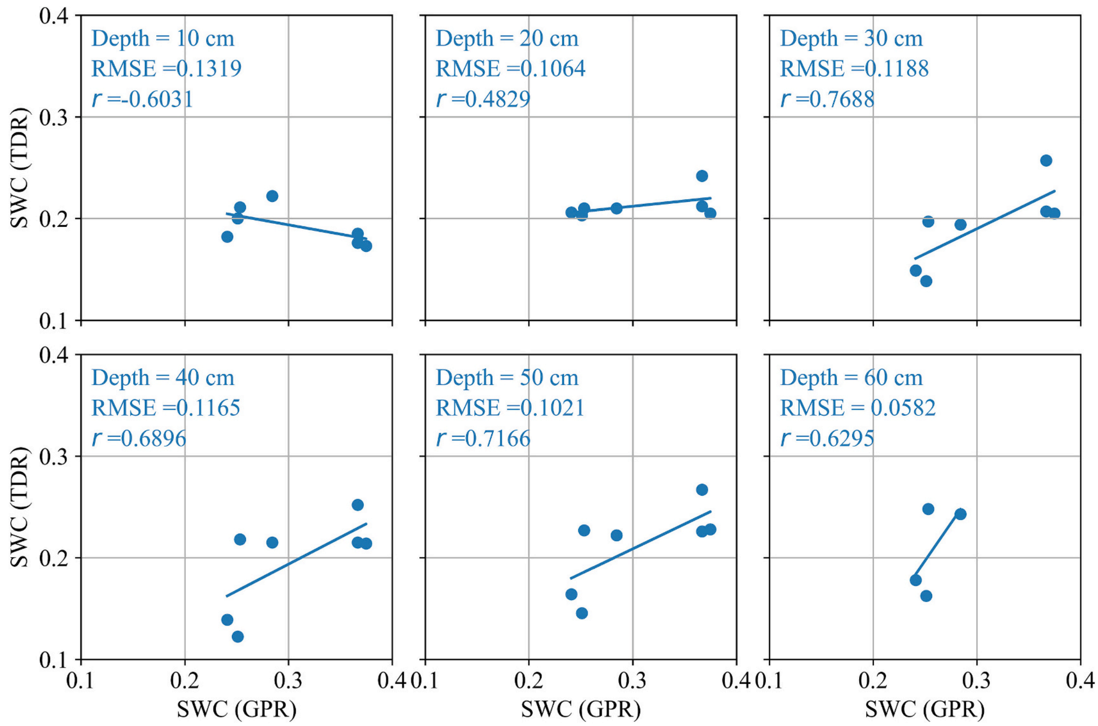

Fig. 10. Comparison of soil volumetric water content (SWC, dimensionless) measured by the drone-borne GPR and TDR sensors at different depths. The RMSE and correlation coefficient (r) between the two measurements are provided. Note that the GPR and TDR measurements were not acquired at exactly the same locations, with estimated horizontal offsets of a few meters, which contribute to the observed differences given the inherent variability in the field.

not influenced by precipitation, making it comparable to a numerically modeled result. The BRT prediction was based on the slope (Fig. 5(a)), altitude (Fig. 5(b)), flow accumulation index (Fig. 5(c)), and soil electrical conductivity (Fig. 6).

The field exhibits a general slope from south to north, with a height difference of approximately 13 m between the highest and lowest points. Despite this overall slope, local slopes within the field remain below 10°. Areas of high flow accumulation and high conductivity are spatially similar, primarily located along the western edge of the site, with some branches of flow extending toward the north. Conversely, most of the low conductivity areas are situated in the southern part of the site.

A comparison of the SWC maps from the drone-borne GPR and BRT prediction is presented in Fig. 11. It is important to note that the only difference between the GPR-derived SWC map in Fig. 7(f) and Fig. 11(a) is the scale and range of the color bar. Fig. 12 shows a quantitative comparison of SWC measured by the drone-borne GPR and predicted by the BRT model.

Visual inspection of Fig. 11 reveals wet areas along the northwestern edge in both maps. However, a wet region extending from the northwest to the southeast is clearly visible in the GPR-derived map (Fig. 11(a)) but is less distinct in the BRT-predicted map (Fig. 11(b)), where the wettest area appears more centered within the site.

Quantitative analysis shows a self RMSE of 0.0258 and a good self-correlation coefficient of 0.602 between the two maps (Fig. 12). However, when calculated using spatial cross-validation, the correlation coefficient decreases to 0.338 ± 0.068 (Table 1), and the regression slope deviates from the 1:1 line. This discrepancy may be partly explained by the well-known fact that soil moisture tends to exhibit greater spatial variability under intermediate moisture conditions, which typically prevail during the growing season and are captured in this study.

4.3.2. Comparison with rainfall and irrigation collection

The second soil water content (SWC) map of interest is the one measured on September 15th (Fig. 7(g)), as it follows rainfall and irrigation events that occurred shortly before this date (see Fig. 8). Fig. 13 presents the SWC map alongside rainfall and irrigation data collected on September 14th and 15th by rain gauges installed on the test site (shown as white dots in Fig. 4). A strong correspondence is observed between the SWC values and the rainfall and irrigation amounts recorded by the rain gauges, with a correlation coefficient of 0.78 (see Fig. 14). It is worth noting that the rain gauge readings indicating 0 mm of water are not outliers but reflect areas that were neither irrigated nor affected by rainfall during the period of interest. These values are crucial for understanding natural soil moisture variability across the field. For instance, relatively high SWC values in non-irrigated zones (such as the talweg in the northwest) are consistently observed, underscoring the influence of topography and soil texture. Including these zero-precipitation points in the correlation analysis thus provides a more complete picture of the spatial heterogeneity and hydrological processes at play across the field.

As shown in Fig. 13, there is an overlap between irrigation lanes labeled as "a" and "b." At the time of the GPR measurement, lanes "a" and "b" had already been irrigated, while lane "c" had not. Consequently, the SWC values are higher in lanes "a" and "b" compared to other areas of the field. In the overlapping region of lanes "a" and "b," the SWC values are even higher due to the combined effect of the overlapping irrigation.

Additionally, the talweg located in the northwest portion of the field, above lane "a," was not irrigated but appears wetter naturally. This consistently wetter area, observed on other measurement dates as well, is linked to the site's topographical characteristics. Finally, the slight spatial shift observed in the wetter areas relative to the expected irrigation zones is most likely due to wind drift from the irrigation cannons, rather than measurement or GPS errors.

5. Conclusions and perspectives

In this study, we applied the gprSense® GPR system, mounted on a drone and integrating a previously validated full-wave inversion method

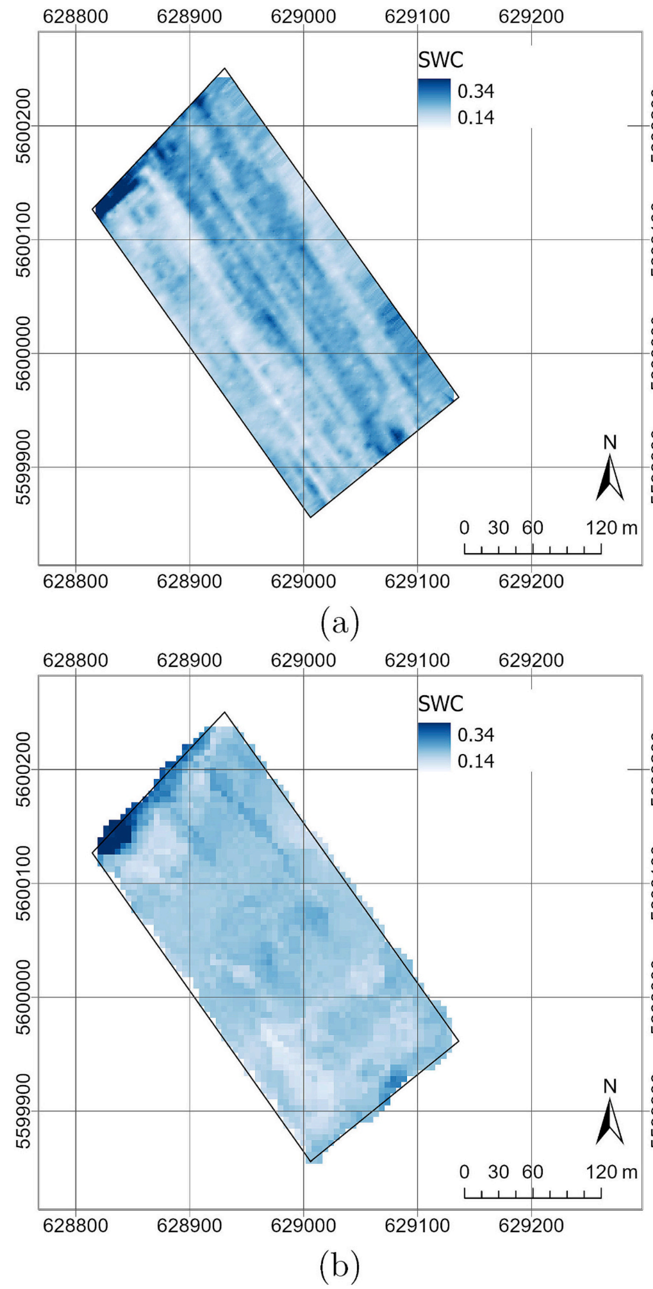

Fig. 11. Soil volumetric water content (SWC) maps measured by the drone-borne GPR on September 11th (a) and predicted by the BRT model (b). Coordinates are in WGS 1984-UTM Zone 31 N.

([Lambot et al., 2004](#)), to monitor root-zone soil water content (SWC) in a spinach field over an entire growing season. Operating within the frequency range of 110–120 MHz, the radar achieved a characterization depth of approximately 35–40 cm. Results were compared with independent ground-based measurements, including SWC values from TDR sensors installed at three positions and six depths. A strong correlation was observed between GPR-derived SWC and TDR measurements at 30–40 cm depth ($r = 0.77$ at 30 cm), consistent with the radar's estimated characterization depth. The number of TDR measurements was necessarily limited due to the practical challenges of deploying point-based sensors in an operational crop field. In addition, the measurements were not colocated because the metallic rods of the TDR probes can perturb the radar signal. As a result, the RMSE values ranged from 0.0582 to 0.1319 across depths. While the lowest RMSE was 0.0582, the value at 30 cm depth (RMSE = 0.1188) is particularly relevant, as it is

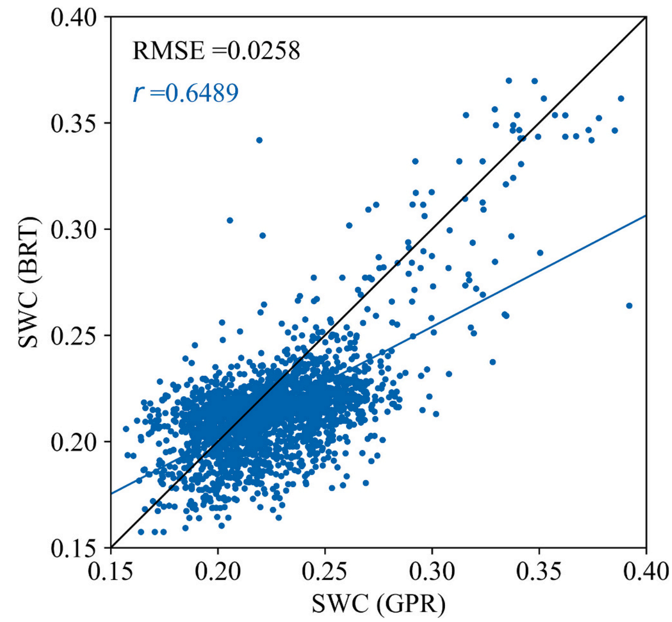

Fig. 12. Comparison of soil volumetric water content (SWC) measured by the drone-borne GPR and predicted by the BRT model.

Table 1
Self-statistics (Self) and cross-validation (CV) statistics (Pearson correlation coefficient and Root Mean Square Error, RMSE) used to evaluate the performance of the Boosted Regression Trees (BRT) model. The standard deviation quantifies the variability of the results across cross-validation folds.

	RSME	Correlation
Self	0.029	0.602
CV	0.032 ± 0.003	0.338 ± 0.068

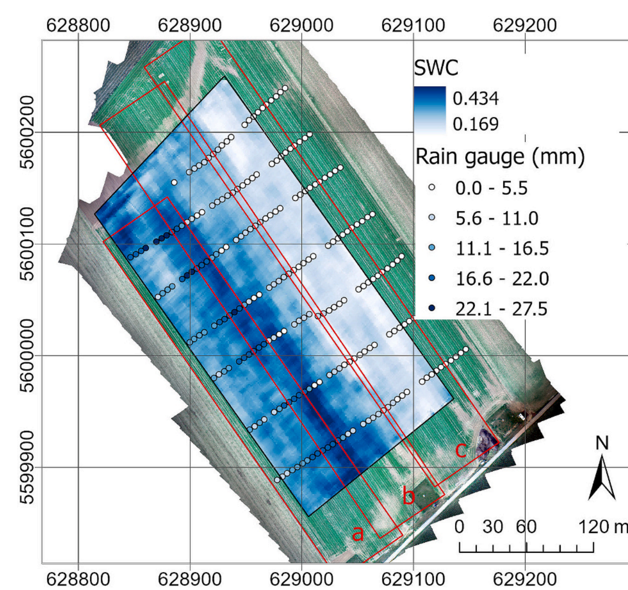

Fig. 13. Soil volumetric water content (SWC) map measured by the drone-borne GPR on September 15th, along with rainfall and irrigation volumes collected by rain gauges on September 14th and 15th. The rectangles labeled"a,""b," and"c" indicate the irrigation areas recorded by the Raindancer system. Lanes"a" and"b" had been irrigated prior to the GPR measurement, while lane"c" had not. Coordinates are in WGS 1984-UTM Zone 31 N.

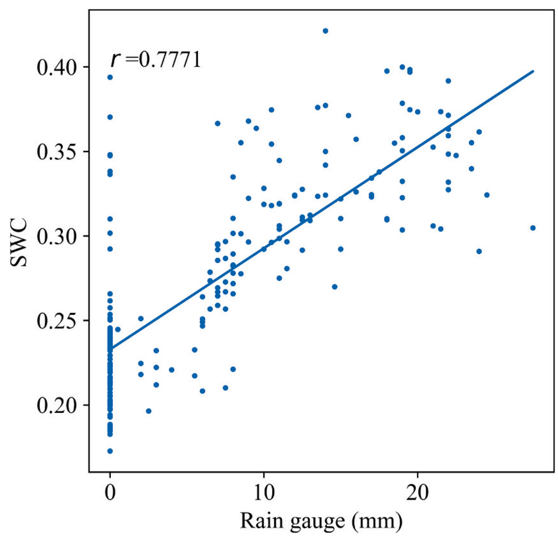

Fig. 14. Comparison of soil volumetric water content (SWC) measured by the drone-borne GPR on September 15th and rainfall and irrigation volumes collected by rain gauges on September 14th and 15th.

consistent with the radar's estimated characterization depth. These values partly reflect natural meter-scale soil heterogeneity rather than GPR inaccuracy. The TDR data were primarily used to support spatial and temporal trends in the GPR-derived maps, rather than to revalidate the inversion model, which has already been comprehensively established in previous studies. Additional comparisons were made with independent data sources. For instance, the GPR-derived SWC map from September 11th was compared with a map predicted using the Boosted Regression Trees (BRT) model, yielding an RMSE of 0.0258. Additionally, the GPR-derived SWC map from September 15th was compared with rainfall and irrigation data collected by rain gauges on September 14th and 15th, resulting in a correlation coefficient of 0.7771. These comparisons support the consistency and reliability of the gprSense® system for characterizing root-zone SWC at the field scale.

This study highlights the potential of drone-borne GPR as a tool to automatically generate high-resolution, time-lapse SWC maps, offering valuable insights into soil moisture dynamics in agricultural landscapes. Comparisons with in-situ sensors and field observations further support the reliability of the retrieved SWC estimates. Long-term monitoring could help refine measurement techniques and improve interpretation of GPR-derived maps under diverse climatic and agronomic conditions.

Although the present study focused on a single agricultural field with spinach, the test site exhibits strong spatial variability in soil texture and slope, and the time-lapse campaign captured a range of meteorological conditions. Importantly, earlier versions of the gprSense® system have already been successfully deployed in contrasting agri-environmental contexts, demonstrating its applicability beyond the present field campaign. Notably, Wu et al. (2022) applied the radar on an irrigation robot for precise irrigation of trench-hill potato fields, and Henrion et al. (2025) demonstrated its drone-borne deployment for year-round soil moisture monitoring in peatlands. These applications confirm the system's versatility and robustness across varying crops, field architectures, and ecosystems. More generally, the low-frequency operation (wavelengths of 2.5–2.7 m at 110–120 MHz) makes it largely insensitive to most crop canopies and surface roughness, making the approach broadly transferable across a wide range of crop types and agricultural soils. This scalability indicates that the method can be applied in diverse climatic regions and over multiple growing seasons without major modifications. Slope and extreme topography remain potential limiting factors for drone deployments, as the current inversion framework does not yet fully account for incidence angle effects; addressing this will be an important step for applications in strongly sloping agricultural landscapes (Wu and Lambot, 2022b).

From a broader perspective, drone-borne GPR offers strong complementarity to satellite observations. Current L-band and C-band radar missions retrieve surface soil moisture at relatively coarse resolutions and are strongly affected by vegetation cover and surface roughness, while the present system directly characterizes root-zone (0–40 cm) soil moisture at the field scale. Drone-borne GPR can therefore serve as a bridging tool, providing high-resolution ground-truthing for satellite-based products and facilitating cross-scale integration of soil moisture information.

By enabling precise monitoring of root-zone SWC, drone-borne GPR has the potential to transform precision agriculture, optimizing irrigation practices, conserving water, and ultimately improving crop yields. The root-zone SWC information retrieved from off-ground GPR can be directly used to inform irrigation decisions by quantifying deviations from crop-specific target values, taking into account both soil and crop types (Wu et al., 2022).

In practice, this could be implemented through integration with irrigation scheduling systems or robotic platforms, enabling site-specific water application at the optimal time and depth. While such operational integration was not tested in this study, the results demonstrate that the information required for this step is already retrievable, highlighting a clear pathway to practical implementation. This innovative approach also holds promise for advancing sustainable farming practices and addressing the challenges posed by increasing climatic variability. Future work will investigate multi-year deployments and broader agri-environmental contexts to further establish scalability and operational readiness.

CRediT authorship contribution statement

Kaijun Wu: Writing – review & editing, Writing – original draft, Visualization, Methodology, Investigation, Formal analysis. **Jean Artois:** Writing – review & editing, Methodology, Investigation, Formal analysis. **Denis Tourneur:** Writing – review & editing, Methodology, Investigation, Formal analysis. **Merlin Mareschal:** Writing – review & editing, Methodology, Investigation, Formal analysis. **Maud Henrion:** Writing – review & editing, Methodology, Investigation, Formal analysis. **Sashini Pathirana:** Methodology, Formal analysis. **Lakshman Galagedara:** Methodology, Formal analysis. **Quentin Limbourg:** Writing – review & editing, Methodology, Investigation, Funding acquisition, Conceptualization. **Sébastien Lambot:** Writing – review & editing, Writing – original draft, Visualization, Methodology, Investigation, Funding acquisition, Formal analysis, Conceptualization.

Declaration of competing interest

The authors declare the following financial interests/personal relationships thatmay be considered as potential competing interests: Sébastien Lambot is also affiliated with Sensar Consulting, which developed the prototype *gprSense*® system used in this study. The development of *gprSense*® was supported by the agROBOfood (MIRAGE, Grant Agreement No. 825395) and ICAERUS (gprSense®, Grant Agreement No. 101060643) projects, funded by the European Union's Horizon Europe research and innovation programme. All other authors declare that they have no known competing financial interests or personal relationships that could have appeared to influence the work reported in this paper.

Acknowledgments

The DuraTechFarm project (Contract No. D65-7390) was funded by the Région Wallonne (Belgium), with additional support from the Fonds de la Recherche Scientifique (FNRS, Belgium). The development of gprSense® (www.gprsense.com) by Sébastien Lambot was supported by the agROBOfood Project (MIRAGE, Grant Agreement No. 825395) and the ICAERUS Project (gprSense®, Grant Agreement No. 101060643) through their Open Calls, funded by the European Union's Horizon Europe Research and Innovation Program.

Data availability

Data will be made available on request.

References

Anh Phuong, T., Andre, F., Lambot, S., 2014. Validation of near-field ground-penetrating radar modeling using full-wave inversion for soil moisture estimation. In: IEEE Transactions on Geoscience and Remote Sensing, 52, pp. 5483–5497. https://doi.org/10.1109/tgrs.2013.2289952. URL: <GotoISI>://WOS:000337171900018.

Bauer-Marschallinger, B., Freeman, V., Cao, S., Paulik, C., Schaufler, S., Stachl, T., Modanesi, S., Massari, C., Ciabatta, L., Brocca, L., Wagner, W., 2019. Toward global soil moisture monitoring with sentinel-1: harnessing assets and overcoming obstacles. IEEE Trans. Geosci. Remote Sens. 57, 520–539. https://doi.org/10.1109/TGRS.2018.2858004.

Bwambale, E., Abagale, F.K., Anornu, G.K., 2022. Smart irrigation monitoring and control strategies for improving water use efficiency in precision agriculture: a review. Agric. Water Manag. 260, 107324. https://doi.org/10.1016/j.agwat.2021.107324.

Chatterjee, S., Desai, A.R., Zhu, J., Townsend, P.A., Huang, J., 2022. Soil moisture as an essential component for delineating and forecasting agricultural rather than meteorological drought. Remote Sens. Environ. 269, 112833. https://doi.org/10.1016/j.rse.2021.112833.

Cheng, Q., Su, Q., Binley, A., Liu, J., Zhang, Z., Chen, X., 2023. Estimation of surface soil moisture by a multi-elevation uav-based ground penetrating radar. Water Resour. Res. 59, e2022WR032621. https://doi.org/10.1029/2022WR032621.

Chew, W.C., 1995. Waves and Fields in Inhomogeneous Media. IEEE Press, Piscataway, NJ.

Dobriyal, P., Qureshi, A., Badola, R., Hussain, S.A., 2012. A review of the methods available for estimating soil moisture and its implications for water resource management. J. Hydrol. 458-459, 110–117. https://doi.org/10.1016/j.jhydrol.2012.06.021.

El Hajj, M., Baghdadi, N., Zribi, M., Bazzi, H., 2017. Synergic use of sentinel-1 and sentinel-2 images for operational soil moisture mapping at high spatial resolution over agricultural areas. Remote Sens 9. https://doi.org/10.3390/rs9121292.

Elith, J., Leathwick, J.R., Hastie, T., 2008. A working guide to boosted regression trees. J. Anim. Ecol. 77, 802–813. https://doi.org/10.1111/j.1365-2656.2008.01390.x.

Ercoli, M., Di Matteo, L., Pauselli, C., Mancinelli, P., Frapiccini, S., Tale-Galli, L., Cannata, A., 2018. Integrated GPR and laboratory water content measures of sandy soils: from laboratory to field scale. Constr. Build. Mater. 159, 734–744. https://doi.org/10.1016/j.conbuildmat.2017.11.082. URL. https://www.sciencedirect.com/science/article/pii/S0950061817322912.

Evrard, O., Vandaele, K., Bielders, C., Wesemael, B.V., 2008. Seasonal evolution of runoff generation on agricultural land in the belgian loess belt and implications for muddy flood triggering. Earth Surf. Process. Landf. 33, 1285–1301. https://doi.org/10.1002/esp.1613.

Falloon, P., Jones, C.D., Ades, M., Paul, K., 2011. Direct soil moisture controls of future global soil carbon changes: an important source of un- certainty. Glob. Biogeochem. Cycles 25. https://doi.org/10.1029/2010GB003938.

Frid, M., Frid, V., 2024. Vital views into drone-based GPR application: precise mapping of soil-to-rock boundaries and ground water level for foundation engineering and site-specific response. Appl. Sci. 14. https://doi.org/10.3390/app14177889. URL. https://www.mdpi.com/2076-3417/14/17/7889.

Galagedara, L.W., Parkin, G.W., Redman, J.D., 2003. An analysis of the GPR direct ground wave method for soil water content measurement. Hydrol. Process. 17, 3615–3628.

Henrion, Maud, Li, Yanfei, Kaijun, Wu, Jonard, François, Opfergelt, Sophie, Vanacker, Veerle, Van Oost, Kristof, Lambot, Sébastien, 2025. Drone-borne ground-penetrating radar reveals spatiotemporal moisture dynamics in peatland root zones. Sci. Remote Sens., 100311 https://doi.org/10.1016/j.srs.2025.100311.

Huisman, J.A., Hubbard, S.S., Redman, J.D., Annan, A.P., 2003. Measuring soil water content with ground penetrating radar: a review. Vadose Zone J. 2, 476–491.

Klotzsche, A., Jonard, F., Looms, M., van der Kruk, J., Huisman, J., 2018. Measuring soil water content with ground penetrating radar: a decade of progress. Vadose Zone J. 17, 180052. https://doi.org/10.2136/vzj2018.03.0052.

Lambot, S., André, F., 2014. Full-wave modeling of near-field radar data for planar layered media reconstruction. IEEE Trans. Geosci. Remote Sens. 52, 2295–2303. https://doi.org/10.1109/TGRS.2013.2259243.

Lambot, S., Slob, E.C., van den Bosch, I., Stockbroeckx, B., Vanclooster, M., 2004. Modeling of ground-penetrating radar for accurate characterization of subsurface electric properties. IEEE Trans. Geosci. Remote Sens. 42, 2555–2568.

Lambot, S., Antoine, M., Vanclooster, M., Slob, E.C., 2006a. Effect of soil roughness on the inversion of off-ground monostatic gpr signal for non- invasive quantification of soil properties. Water Resour. Res. 42, W03403. https://doi.org/10.1029/2005WR004416.

Lambot, S., Weihermüller, L., Huisman, J.A., Vereecken, H., Vanclooster, M., Slob, E.C., 2006b. Analysis of air-launched ground-penetrating radar techniques to measure the soil surface water content. Water Resour. Res. 42. https://doi.org/10.1029/2006WR005097.

Lambot, S., Slob, E., Chavarro, D., Lubczynski, M., Vereecken, H., 2008. Measuring soil surface water content in irrigated areas of southern Tunisia using full-waveform inversion of proximal GPR data. Near Surf. Geophys. 6, 403–410. URL: <GotoISI>://000261736100007.

Mahmoudzadeh Ardekani, M.R., 2013. Off- and on-ground GPR techniques for field-scale soil moisture mapping. Geoderma 200-201, 55–66. https://doi.org/10.1016/j.geoderma.2013.02.010.

Minet, J., Bogaert, P., Vanclooster, M., Lambot, S., 2012. Validation of ground penetrating radar full-waveform inversion for field scale soil moisture mapping. J. Hydrol. 424-425, 112–123. https://doi.org/10.1016/j. jhydrol.2011.12.034.

Misra, G., Cawkwell, F., Wingler, A., 2020. Status of phenological re- search using sentinel-2 data: a review. Remote Sens 12. https://doi.org/10.3390/rs12172760.

Paloscia, S., Pettinato, S., Santi, E., Notarnicola, C., Pasolli, L., Reppucci, A., 2013. Soil moisture mapping using sentinel-1 images: algorithm and preliminary validation. Remote Sens. Environ. 134, 234–248. https://doi.org/10.1016/j.rse.2013.02.027.

Pathirana, S., Lambot, S., Krishnapillai, M., Cheema, M., Smeaton, C., Galagedara, L., 2023. Ground-penetrating radar and electromagnetic in- duction: challenges and opportunities in agriculture. Remote Sens 15. https://doi.org/10.3390/rs15112932.

Pramudita, A.A., Wahyu, Y., Rizal, S., Prasetio, M.D., Jati, A.N., Wu-Lansari, R., Ryanu, H.H., 2022. Soil water content estimation with the presence of vegetation using ultra-wideband radar-drone. IEEE Access 10, 85213–85227. https://doi.org/10.1109/ACCESS.2022.3197636.

Seyedmohammadi, J., Esmaeelnejad, L., Ramezanpour, H., 2016. Land suitability assessment for optimum management of water consumption in precise agriculture. Model. Earth Syst. Environ. 2, 1–11. https://doi.org/10.1007/s40808-016-0212-9.

Sharma, P.K., Kumar, D., Srivastava, H.S., Patel, P., 2018. Assessment of different methods for soil moisture estimation: a review. J. Remote Sens. GIS 9, 57–73.

Sipos, D., Gleich, D., 2020. A lightweight and low-power UAV-borne ground penetrating radar design for landmine detection. Sensors 20. https://doi.org/10.3390/s20082234. URL. https://www.mdpi.com/1424-8220/20/8/2234.

Slob, E.C., Fokkema, J., 2002. Coupling effects of two electric dipoles on an interface. Radio Sci. 37, 1073. https://doi.org/10.1029/2001RS2529.

Tarboton, D.G., 1997. A new method for the determination of flow directions and upslope areas in grid digital elevation models. Water Resour. Res. 33, 309–319. https://doi.org/10.1029/96WR03137.

Topp, G.C., Davis, J.L., Annan, A.P., 1980. Electromagnetic determination of soil water content: measurements in coaxial transmission lines. Water Resour. Res. 16, 574–582. https://doi.org/10.1029/WR016i003p00574.

Tran, A.P., Bogaert, P., Wiaux, F., Vanclooster, M., Lambot, S., 2015. High- resolution space-time quantification of soil moisture along a hillslope using joint analysis of ground penetrating radar and frequency domain reflectometry data. J. Hydrol. 523, 252–261. https://doi.org/10.1016/j.jhydrol.2015.01.065. URL: ://WOS:000351971700023.

Valavi, R., Elith, J., Lahoz-Monfort, J.J., Guillera-Arroita, G., 2019. Blockcv: an r package for generating spatially or environmentally separated folds for k-fold cross-validation of species distribution models. Methods Ecol. Evol. 10, 225–232. https://doi.org/10.1111/2041-210X.13107. URL. https://besjournals.onlinelibrary.wiley.com/doi/abs/10.1111/2041-210X.13107.

Valence, E., Baraer, M., Rosa, E., Barbecot, F., Monty, C., 2022. Drone- based ground-penetrating radar (GPR) application to snow hydrology. Cryosphere 16, 3843–3860. https://doi.org/10.5194/tc-16-3843-2022. URL. https://tc.copernicus.org/articles/16/3843/2022/.

Varghese, D., Radulovi`c, M., Stojkovíc, S., Crnojevíc, V., 2021. Reviewing the potential of sentinel-2 in assessing the drought. Remote Sens 13. https://doi.org/10.3390/rs13173355.

Vereecken, H., Huisman, J.A., Bogena, H., Vanderborght, J., Vrugt, J.A., Hopmans, J.W., 2008. On the value of soil moisture measurements in vadose zone hydrology: a review. Water Resour. Res. 44. https://doi.org/10.1029/2008WR006829.

Wallace, A., 1994. High-precision agriculture is an excellent tool for conservation of natural resources. Commun. Soil Sci. Plant Anal. 25, 45–49.

Wu, K., Lambot, S., 2022a. Analysis of low-frequency drone-borne GPR for root-zone soil electrical conductivity characterization. IEEE Trans. Geosci. Remote Sens. 60, 1–13. https://doi.org/10.1109/TGRS.2022. 3198431.

Wu, K., Lambot, S., 2022b. Effect of radar incident angle on full-wave inversion for the retrieval of medium surface permittivity for drone-borne applications. IEEE Trans. Geosci. Remote Sens. 60, 1–10. https://doi.org/10.1109/TGRS.2022.3157370.

Wu, K., Rodriguez, G.A., Zajc, M., Jacquemin, E., Clément, M., De Coster, A., Lambot, S., 2019. A new drone-borne GPR for soil moisture mapping. Remote Sens. Environ. 235, 111456. https://doi.org/10.1016/j.rse.2019.111456.

Wu, K., Desesquelles, H., Cockenpot, R., Guyard, L., Cuisiniez, V., Lambot, S., 2022. Ground-penetrating radar full-wave inversion for soil moisture mapping in trench-hill potato fields for precise irrigation. Remote Sens 14. https://doi.org/10.3390/rs14236046.

Yavkacheva, Z., 2023. Importance of soil moisture in agriculture. Sci. Innov. 2, 211–217. https://doi.org/10.5281/zenodo.7982648.

Zhou, L., Yu, D., Wang, Z., Wang, X., 2019. Soil water content estimation using high-frequency ground penetrating radar. Water 11. https://doi.org/10.3390/w11051036. URL. https://www.mdpi.com/2073-4441/11/5/1036.